Trends in opto-electronic properties of $Mg_xZn_{1-x}SnN_2$ using first principles methods

B.B. Dumre [a], R.J. Nelson [b], R.E. Irving [a], R.J. Ellingson [a], S.V. Khare [a],*

[a] Department of Physics and Astronomy, and Wright Center for Photovoltaics Innovation and Commercialization (PVIC), University of Toledo, Toledo, OH, 43606, USA
[b] Department of Mathematics, Southern Utah University, Cedar City, UT, 84720, USA

HIGHLIGHTS

- Crystal structure for $Mg_xZn_{1-x}SnN_2$ simulated using special quasi-random structures (SQS).
- Opto-electronic properties of computed with the hybrid HSE06 functional.
- Hole effective masses lower than electron effective masses.
- Band gaps increase with increase in Mg concentration.
- Substantial absorption with lower reflectivity.

ARTICLE INFO

ABSTRACT

We have computationally studied $Mg_xZn_{1-x}SnN_2$ alloy system in wurtzite structure using density functional theory and beyond. Cationic disorder of the random limit is chosen for modeling the crystal structure. Lattice mismatch of less than 1 % in the alloy system helps in the miscibility of Mg and Zn, thus making it widely useful in tandem solar cells. Electronic band gaps increase linearly with higher Mg concentration. These materials have hole effective masses significantly lower than electron effective masses. Considerable absorption together with a lower reflectivity can render this alloy an effective absorber. All the alloys are mechanically stable, but ($x = 0.25$) and ($x = 0.50$) are dynamically unstable. These alloys also exhibit large hardness.

1. Introduction

In a single junction solar cell, the bandgap range of $\sim$ (1.1–1.4) eV in an absorber material layer is considered optimal to obtain a maximum efficiency of approximately 33 % according to Shockley-Queisser Limit [1]. Moreover, any other bandgaps of interest can be utilized for multi-junction tandem solar cells. For example, in a three-junction solar cell design, arbitrary materials with band gap combination of 1.91 eV / 1.37 eV / 0.93 eV for top / middle / base cell model has been simulated theoretically to increase the efficiency up to 52% [2].

In this context, $In_xGa_{1-x}N$, an example of group-III-N nitrides, have their bandgaps spanning from 0.7 eV for InN to 3.5 eV for GaN, which can encompass the electromagnetic spectrum from near infra-red to ultra-violet [3]. Thus, this alloy has been utilized to produce a better tandem design in solar cells along with light emitting diodes and laser diodes [4,5]. However, higher In content in $In_xGa_{1-x}N$ is immiscible due

to a large lattice mismatch of 10 % between InN and GaN [6]. This creates the bandgap of green light of (2.19–2.48) eV range inaccessible [7]. To tackle this "green gap" issue, group-II-IV-N_2 ternary nitrides have been proposed in the last decade [8]. These II-IV-N_2 semiconductors also mitigate defects by inserting group II metals in the metal site vacancies observed in III-N semiconductors [9]. Out of them, $Zn(Si,Ge)N_2$ alloys span their bandgaps from 4.5 eV ($ZnSiN_2$) to 3.2 eV ($ZnGeN_2$), and thus are wide bandgap semiconductors [10,11]. Similarly, $Zn(Ge,Sn)N_2$ alloys span their bandgaps from 3.1 eV ($ZnGeN_2$) to 2.0 eV ($ZnSnN_2$), and include the aforementioned green light region without having the problem of miscibility gap [12]. However, the presence of Ge in this alloy system makes it an expensive contender [13]. Ultimately, $Mg_xZn_{1-x}SnN_2$ alloys are anticipated to manifest bandgaps in the range of 1.0 eV ($ZnSnN_2$) to 2.7 eV ($MgSnN_2$), which also can solve the "green gap" problem without any miscibility issues by using earth abundant, non-toxic and easily recyclable metals Mg, Zn and Sn [13–15].

$Mg_xZn_{1-x}SnN_2$ alloys have been recently grown experimentally on GaN(001) substrate by Yamada et al. in wurtzite structure [13]. As stated in the earlier paragraph, this alloy system is miscible in all concentration range (x = 0–1) unlike $In_xGa_{1-x}N$, as the lattice mismatch between end members is less than 1% in both in- and out-of-the-plane directions [13]. Even though bandgap range is contended to span from 1.0 eV to 2.7 eV by Yamada et al. [13], bandgap tunability have been expected in a different range of 1.12 eV–3.43 eV according to Makin et al. as explained in their work related to bandgap engineering by exploiting cation disorder [15]. The end members of $Mg_xZn_{1-x}SnN_2$ alloy system have been studied recently by different research groups with varying bandgap results subjected to different experimental and theoretical conditions [10,16–36]. A comprehensive study of $Mg_xZn_{1-x}SnN_2$ alloy system spanning the whole composition (x) range is lacking. A study of general trend of opto-electronic properties is necessary at this stage to further assess the applicability of $Mg_xZn_{1-x}SnN_2$ alloy system. Hence, we have utilized the high accuracy rendering HSE06 functional to compute the opto-electronic properties for $Mg_xZn_{1-x}SnN_2$ alloy in all the composition (x) range along with structural, mechanical, and vibrational properties.

In this work, we have calculated various physical properties of $Mg_xZn_{1-x}SnN_2$ alloy system in wurtzite crystal structure using Density Functional Theory (DFT) and beyond. We have tried to establish trends in those physical properties calculated. Our results remain predictive for future endeavors. We have utilized only the most random version of the disorders observed in the crystal structures for this study. The issue of immiscibility is solved in this alloy due to the small lattice mismatch of less than 1 %. All the alloys are mechanically stable, but ($x = 0.25$) and ($x = 0.50$) are vibrationally unstable. Phonon-phonon interactions may stabilize these materials at room temperature. Band gaps have a linear upward trend with Mg concentration. Hole effective masses are lower than electron effective masses in these materials. Substantial absorption with a lower reflectivity makes this alloy an efficacious absorber. Superhard behavior is found in the alloys.

2. Computational methods

All the DFT and beyond computations were executed on Vienna Ab initio Simulation Package (VASP) [37–40]. The Perdew–Burke–Ernzerhof (PBE) [41,42] Generalized Gradient Approximation (GGA) exchange-correlation functional was implemented in the Projector-Augmented-Wave (PAW) method [40,43]. Semi-core electrons were also involved in the approximation of electron density in addition to the outer core. PAW PBE VASP pseudopotentials, i.e., 'Mg_sv', 'Zn', 'Sn_d', and 'N_s', were used along with the cut-off energy of plane waves of 500 eV to ensure the accuracy of the calculations [44–46]. 4000 k-points per reciprocal atom (KPPRA) with a Γ-centered k-point mesh was utilized in our calculations [47–50]. Each atom was structurally relaxed until the forces were under 0.01 eV/Å, and the convergence criterion of energy in electronic iterations of 10^{-6} eV/atom was set when deploying a Gaussian smearing of width 0.05 eV [51–54]. The number of empty bands in the conduction band were 20% of the valence band for each material for the calculation of accurate result of material properties. At the beginning, initial crystal structures were obtained from the Materials Project [55]. To calculate random Mg/Zn occupation occurring in a disordered crystal structure, Special Quasirandom Structures (SQS) [56–58] were generated using the mcsqs code within ATAT [59–63]. To simulate plausible random configurations in the alloys of $Mg_xZn_{1-x}SnN_2$, SQS were constructed from 2 × 2 × 2 supercells of the conventional wurtzite unit cells (Space Group $P6_3mc$) at concentrations of x = 0.00, 0.25, 0.50, 0.75, and 1.00.

Atomic positions, cell shape, and cell volume were relaxed while optimizing the geometry of the crystal structures. Presence of magnetic properties was also assessed during the geometry optimization process. After relaxation, high-precision static calculations were performed to calculate the accurate ground-state energies of the reactants and products to calculate formation energy. Formation energy per formula unit of $Mg_xZn_{1-x}SnN_2$ was calculated as [64–66]:

$$\Delta E_f = E(Mg_xZn_{1-x}SnN_2) - xE(Mg) - (1-x)E(Zn) - E(Sn) - E(N_2) \quad (1)$$

where E(Mg), E(Zn), E(Sn), and E(N_2) are the ground-state energies of magnesium (space group: $P6_3/mmc$), zinc (space group: $P6_3/mmc$), tin (space group: $I4_1/amd$), and nitrogen dimer in vacuo, respectively.

Elastic constants were calculated using strained supercells by computing the Hessian matrices of directional second derivatives of energy with respect to cell distortion using finite differences [65,67–74]. For each structure, the average bulk (B) and shear (G) moduli were derived from the elastic tensor (C_{ij}) by utilizing the Voigt–Reuss–Hill [20,51,75–80] method. Pugh's ratio and Vickers hardness are obtained as discussed by Pugh [81] and Tian et al. [82–85] as:

$$\kappa = G/B \text{ and } H_V = 0.92\kappa^{1.137}G^{0.708}, \text{respectively.} \quad (2)$$

The mechanical stability of each structure in wurtzite crystal structure was assessed by determining the positive definiteness of C_{ij} described by Born criteria [86] as:

$$C_{11} > |C_{12}|, 2C_{13}^2 < C_{33}(C_{11} + C_{12}), C_{44} > 0, \text{and } C_{66} > 0. \quad (3)$$

Electronic band gaps of solid-state semi-conductor materials are underestimated by the GGA exchange-correlation functional [87]. Thus, in such calculations, we implemented the Heyd–Scuseria–Ernzerhof (HSE06) hybrid functional [88], which integrates 25 % of the exact exchange from Hartree–Fock theory, and 75 % of the exchange-correlation from GGA. In the context of semiconductors and insulators, this functional has been able to predict experimental results more accurately [69,87,89,90]. Thus, by utilizing HSEO6 functional, we have computed the electronic density of states (DOS), band structure, and frequency-dependent complex dielectric function ($\varepsilon_1 + i\varepsilon_2$) for $Mg_xZn_{1-x}SnN_2$ alloys [91]. By using complex dielectric function, we have derived absorption coefficient (α) and reflectivity (r) [92] as:

$$\alpha = \frac{4\pi k}{\lambda} \text{ and } r = \frac{(n-1)^2 + k^2}{(n+1)^2 + k^2}, \text{respectively; where extinction coefficient}$$

$$(k) = \sqrt{\frac{\sqrt{\varepsilon_1^2 + \varepsilon_2^2} - \varepsilon_1}{2}}, \lambda \text{ is the wavelength of photon, and refractive index}$$

$$(n) = \sqrt{\frac{\sqrt{\varepsilon_1^2 + \varepsilon_2^2} + \varepsilon_1}{2}}. \quad (4)$$

Band structure calculation was utilized to calculate effective masses (m^*) of holes ($m_h^* = m_h/m_o$) and electrons ($m_e^* = m_e/m_o$) using the BoltzTrap2 [93,94] package evaluated in room temperature (300 K) with constant relaxation time approximated to be 10^{-14} s, where m_h is the mass of hole in the lattice, m_e is the mass of electron in the lattice and m_o is the electron rest mass. Two bands at both Valence Band Maximum (VBM) and Conduction Band Minimum (CBM) were considered for calculation of effective masses.

To comprehend the chemical bonding, we calculated Crystal Orbital Hamilton Population (COHP) using the Local-Orbital Basis Suite Towards Electric-structure Reconstruction (LOBSTER) package [66,68,83, 95–101]. Furthermore, to understand the charge transferred in the formation of the compound, we have calculated effective charges on each chemical species by Bader analysis [102–105]. To assess the phonon behavior inside the crystal, we used the Phonopy [106] package to compute phonon DOS for $Mg_xZn_{1-x}SnN_2$ alloys.

Since we want to study various properties of cation-disordered $Mg_xZn_{1-x}SnN_2$ as a function of concentration, let's first define a bowing parameter (δ_p). It helps us to understand the deviation from linearity for any physical quantity (p) such as, bandgap (E_g), effective mass (m^*), or others, as [107]:

$$p_{mix}(x_{Mg}) = x_{Mg}p_{MgSnN_2} + (1 - x_{Mg})p_{ZnSnN_2} - x_{Mg}(1 - x_{Mg})\delta_p, \quad (5)$$

where, x_{Zn} is the percentage of Zn in the alloy and p_{mix}, p_{MgSnN_2}, and p_{ZnSnN_2} are values of the physical quantity associated with the resultant

alloy, MgSnN$_2$, and ZnSnN$_2$ respectively.

3. Results

3.1. Structural and energetic properties

The end members; MgSnN$_2$ and ZnSnN$_2$, and the alloys of Mg$_x$Zn$_{1-x}$SnN$_2$ in the solid state have been mostly studied both experimentally [16,108] and theoretically [20,109] in disordered-wurtzite crystal structure. The end members of the alloy Mg$_x$Zn$_{1-x}$SnN$_2$ have both cations and anions in their respective 2b Wyckoff positions in an ordered wurtzite crystal structure (Space Group $P6_3mc$). However, there are two different atoms in the cationic sublattice of 2b Wyckoff positions in the end members, whereas three different atoms in the cationic sublattice of 2b Wyckoff positions in the alloys. Thus, all the members of the alloy have cationic disorder. Due to the reduction in symmetry in the crystal structure as due to the disorder, the end members take trigonal (Space Group $P3m1$) crystal structure whereas the intermediate members reduce to triclinic (Space Group $P1$). The SQS [56] of cation disordered supercells have 32 atoms in each cell for all the members of the alloy Mg$_x$Zn$_{1-x}$SnN$_2$. The coordination number is 4 as observed ubiquitously in a wurtzite structure with tetrahedral geometry and ABAB… layer stacking. There are various permutations of atomic placements in the Wyckoff positions during the formation of a disordered-wurtzite lattice. We chose the SQS [56] lattice structure in our study for all the members of Mg$_x$Zn$_{1-x}$SnN$_2$ alloys with cationic disorder approaching random limit to conserve computational resources.

Table 1 displays equilibrium lattice constant and formation energy per atom of the Mg$_x$Zn$_{1-x}$SnN$_2$ alloy system calculated using GGA functional. We did not find any magnetic properties of Mg$_x$Zn$_{1-x}$SnN$_2$ alloys. Our computed lattice constants match closely with previous theoretical [20,109] and experimental work [13,23,110]. We have found that the difference between the lattice constants amongst the Mg$_x$Zn$_{1-x}$SnN$_2$ alloys is less than 1 %. Even though the radius of Mg (1.412 Å) and Zn (1.304 Å) in a tetrahedrally coordinated environment are considerably different, the lattice constants being similar can be attributed to the valence electron number of 2 in both Mg and Zn [111]. Table S1 lists average value of bond lengths up to the first nearest neighbors around an element in the Mg$_x$Zn$_{1-x}$SnN$_2$ alloy system. The average bond lengths around each element are nearly constant in each member of the alloy. This explains the miscible nature of the Mg$_x$Zn$_{1-x}$SnN$_2$ alloys as discussed earlier in the second paragraph of section 1. This miscible nature also helps in epitaxial growth of these alloys where variable band gap materials are required as in a tandem solar cell that pacifies the strain energy in between the epitaxial layers. Also, the calculated result of formation energy by using equation (5) is visually displayed in Figure S1a). It declines with increasing Mg

concentration nearly linearly. Approximately up to 10 % of Mg concentration in the alloy requires endothermic chemical reaction to be formed, whereas others are spontaneous.

3.2. Mechanical properties

Values of elastic and mechanical properties such as elastic constants (C$_{ij}$), mechanical stability, bulk modulus (B), shear modulus (G), Pugh's ratio (κ), and Vickers hardness (H$_V$) for the alloys of Mg$_x$Zn$_{1-x}$SnN$_2$ are given in Table S2 calculated using GGA functional. We have calculated for all the members of Mg$_x$Zn$_{1-x}$SnN$_2$ alloys to be mechanically stable according to the Born criteria [86]. Besides the ($x = 0.00$) alloy, the other four members of the Mg$_x$Zn$_{1-x}$SnN$_2$ alloy system have comparable values of C$_{ij}$. The effect is also observed in other derived mechanical properties. The bulk and shear moduli in all the five members decrease in the order: ($x = 0.75$) > ($x = 0.50$) > ($x = 1.00$) > ($x = 0.25$) > ($x = 0.00$). Hence, the $x = 0.75$ member of the alloy is the highly resistive towards bulk and shear deformations. The Pugh's ratio decreases in the five members as: ($x = 0.00$) > ($x = 0.25$) > ($x = 0.50$) = ($x = 0.75$) > ($x = 1.00$). A lower value of Pugh's ratio indicates brittleness, whereas a higher value indicates malleability/ductility [81]. Thus, $x = 0.00$ member of the alloy is more malleable/ductile and $x = 1.00$ is more brittle. The Vickers hardness in all the five members increase in the order: ($x = 0.00$) < ($x = 0.25$) < ($x = 0.50$) < ($x = 1.00$) < ($x = 0.75$). All these values of the mechanical properties are predictive for the future experimental work. The hardness values of these members are higher than that of well-known solar cell materials such as Si (11.77 GPa) [112] and CdTe (0.49 GPa) [113]. Hence, all these members of the alloy will be mechanically suitable for application in solar cell layers. Besides solar usage, these materials are one of the hardest materials comparable to others used in hard-coatings industry such as TiN (25 GPa), ZrC (27 GPa), HfN (20 GPa), TaC (26 GPa) [114–117]. Hence, Mg$_x$Zn$_{1-x}$SnN$_2$ alloy system should be investigated further experimentally as a potential super-hard material as well.

3.3. Vibrational properties

Fig. S2 displays phonon DOS for all the members of Mg$_x$Zn$_{1-x}$SnN$_2$ alloy system calculated using GGA functional. Besides ($x = 0.25$) and ($x = 0.50$), the other three members of the alloy are dynamically stable. The peak phonon DOS value in the imaginary frequency region for vibrationally unstable ones are very small compared to what we observe in the real frequency region. Phonon-phonon interaction at a higher temperature might help both of them to exist experimentally because this current DFT calculates vibrations at 0 K [118]. The ($x = 0.25$) has even smaller value of phonon DOS while compared to what we observe for ($x = 0.50$) at imaginary frequency regime. Hence, we suspect that ($x = 0.25$) might stabilize at a lower temperature than ($x = 0.50$).

Moreover, we observe that N phonon DOS mostly congregate in a higher frequency region, typically around 15 THz. Sn phonon DOS are found in the lowest frequency region around 3 THz. Likewise, Zn is observed around 4 THz, whereas Mg is observed around 10 THz region. This clarifies that the lighter particles have higher vibrational frequencies than the heavier ones. In addition, we observe some gaps in the phonon DOS in all the members of the alloys. These signature gaps are present at around (7.5–9.5) THz in ($x = 0.00$) of value 1.65 THz, around 8 THz of value 0.59 THz and (10–11) THz of value 0.83 THz in ($x = 0.25$), around 10.5 THz of value 0.36 THz and 11.5 THz of value 0.85 THz in ($x = 0.50$), around 11.5 THz of value 0.36 THz and (13–13.5) THz of value 0.36 THz in ($x = 0.75$), and around (11.5–13.5) THz of value 2.27 THz and (17–18) THz of value 1.76 THz in ($x = 1.00$). These phonon gaps make these alloys suitable to be used as sound filters and mirrors as any phonon of frequency within the gap will not penetrate the material and thus will be reflected from the surface [119].

Table 1
Lattice constants, in Å, of Mg$_x$Zn$_{1-x}$SnN$_2$ along with their formation energies per atom, in eV, calculated using the GGA functional. Values from the literature are listed where available.

Material	Space Group	Lattice Constants (Å)		Formation Energy (meV)
		a	c	
ZnSnN$_2$	$P3m1$	3.44, 3.38[a], 3.376(1)[b]	5.58, 5.58[a], 5.467(1)[b]	38.61
Mg$_{0.25}$Zn$_{0.75}$SnN$_2$	$P1$	3.43	5.54	−92.37
Mg$_{0.50}$Zn$_{0.50}$SnN$_2$	$P1$	3.43, 3.43[c]	5.53, 5.51[c]	−194.36
Mg$_{0.75}$Zn$_{0.25}$SnN$_2$	$P1$	3.44	5.52	−246.83
MgSnN$_2$	$P3m1$	3.44, 3.44[d], 3.38 ± 0.04[e]	5.58, 5.58[d], 5.49 ± 0.02[e]	−267.65

[a] Theoretical (Local Density Approximation (LDA)) Ref. [109].
[b] Experimental Ref. [110].
[c] Experimental Ref. [13].
[d] Theoretical (GGA) Ref. [20].
[e] Experimental Ref. [23].

3.4. Electronic properties

Fig. S3 shows the electronic DOS per formula unit for $Mg_xZn_{1-x}SnN_2$ alloys computed using the hybrid HSE06 functional. In the three intermediate members, Zn states dominate in the Valence Band Maximum (VBM), whereas Zn and N states equally dominate in $ZnSnN_2$, and only N states dominate in $MgSnN_2$ in the VBM. Similarly, Zn has a peak in its electronic DOS at around -5 eV in all the four members of the alloys including Zn, which gets shifted more towards VBM as the Mg concentration increases. Finally, in $MgSnN_2$, those states greatly shift and reach near VBM. All the members have a discontinuity in electronic DOS above VBM displaying the characteristic electronic band gap for each. The electronic band gap will be discussed in detail in the upcoming fourth paragraph of this section. In the Conduction Band Minimum (CBM), Sn states are observed dominating DOS.

To elaborate on these results, we have also computed projections of plane waves into local atomic orbitals defined as negative of projected COHP (-pCOHP) using GGA functional for $Mg_xZn_{1-x}SnN_2$ alloy system as shown in Fig. S4. It is a dimensionless quantity, and its positive value means positive bonding, negative value means anti-bonding, and zero means non-bonding. The calculation has been done to include all the interactions between all nearest neighbors. Positive bonding is observed only between Sn–N nearby the VBM in all the members of the alloys. Also, Zn–N interactions have developed anti-bonding states near VBM. Similar to what we observed in electronic DOS as shown in Fig. S3, we observe some positive bonding states created by the interaction of Zn with N around -5 eV region which gradually shifts towards the VBM. Finally, in $MgSnN_2$, the shift is rapid due to the interaction of Mg with N still causing some bonding states. Above the Fermi level, all the nearest neighbor interactions in the conduction band are in anti-bonding states as the electronic states are loosely bound there.

Table S3 displays the charges transferred from Mg, Zn, and Sn to N in all the five members of $Mg_xZn_{1-x}SnN_2$ alloy system calculated using the GGA functional. There is hardly any variation in the charge transferred from the metals to N in each member of the alloy, except from Sn to N in $MgSnN_2$. This could be due to the similarity in lattice constant and bond length as discussed in section 3.1. The exception also could be due to the degree of randomness in the supercell structure selected by SQS approach [56]. All the charges transferred from metal to N are higher than 1 e, hence, we can surmise that bonds are ionic in nature. The ionicity of the bonds in the lattice increases in the order: (Zn–N) < (Mg–N) < (Sn–N). The electronegativities of Mg, Zn, Sn, and N are 1.23 e, 1.66 e, 1.72 e and 3.07 e respectively, based on electrostatic force calculated by Allred et al. [120]. Although the difference between electronegativities of atoms in Mg–N bonds (1.84 e) and Zn–N bonds (1.41 e) are higher than in Sn–N bonds (1.35 e), we speculate that the higher charge-transferred from Sn to N compared to Mg and Zn to N can be attributed to the higher number of valence electrons of 4 in Sn while compared to 2 in Mg and Sn. The average of charge transfer from all the metals to N given in the fifth column of Table S3 increases with the band gap of the alloys.

Bandgaps for all the five members of $Mg_xZn_{1-x}SnN_2$ alloy system calculated using the hybrid HSE06 functional are given in Table 2. All the bandgaps are direct in nature at $\Gamma(0, 0, 0)$ point. As discussed in the third paragraph of section 1, various band gaps for this alloy system have been reported by the earlier work [10,16–36]. We infer this variation is due to the difference in the degree of cationic disorder in the alloys. Our results are for the supercell for each member of the alloy with totally random limit as suggested by the SQS approach [56]. Study of a varying degree of disorder in this alloy system remains a future endeavor. For example, for $MgSnN_2$, we performed a sample run on the ordered orthorhombic structure which is the corresponding ordered structure of a disordered wurtzite lattice [20]. We found that the band gap varied by 0.5 eV as shown in Table 2. For the random limit, the calculated band gap result of 2.73 eV for $ZnSnN_2$ is close to the experimental result of 2.38 eV [108]. Fig. 1a) displays our calculated band

Table 2

Bandgaps, in eV, and effective masses, in standard electron rest mass mo, of $Mg_xZn_{1-x}SnN_2$ calculated using HSE06. Bandgaps calculated using GGA are also given for comparison. Values from the literature are listed where available.

Material	Space Group	Bandgap (eV), Direct	
		GGA	HSE06
$ZnSnN_2$	$P3m1$	0.37	2.73, 2.38[a]
$Mg_{0.25}Zn_{0.75}SnN_2$	$P1$	0.77	3.16
$Mg_{0.50}Zn_{0.50}SnN_2$	$P1$	1.30	3.70, 1.80[b]
$Mg_{0.75}Zn_{0.25}SnN_2$	$P1$	1.28	3.73, 2.20[b]
$MgSnN_2$	$P3m1$	2.47	4.36, 4.86[c], 3.43[d]

[a] Experimental Ref. [108].
[b] Experimental Ref. [13].
[c] Theoretical Ref. (HSE06) [20].
[d] Experimental Ref. [15].

gap result graphically. We observe that there is a linear trend in the band gaps for this alloy system as the Mg concentration changes.

Table S4 provides both electron and hole effective masses in all the five members of $Mg_xZn_{1-x}SnN_2$ alloy system calculated using HSE06 functional. Fig. 1b) shows the effective masses graphically, where we observe upward bowing in both charge carrier effective masses. The bowing parameter for electron and hole effective masses were calculated to be -57.47 m_o and -0.56 m_o using equation (5). The value of hole effective masses is lower than electron effective masses. However, all the charge carrier effective masses are higher than the effective mass for Si ($m_e^* = 1.06$, $m_h^* = 0.59$) [121]. The mobility in these alloys can be degraded by the possibility of further alloy scattering [122]. Except for ($x = 0.25$) in hole effective masses, all other charge carrier effective masses have standard deviation value lower than their own magnitude.

3.5. Optical properties

The dielectric constants for all the five members of $Mg_xZn_{1-x}SnN_2$ alloy system calculated using HSE06 functional is given in Table S5. It has been graphically displayed in Figure S1b). The trend in dielectric constants is nearly linear with concentration, x. The average of two directions is considered while calculating these results in dielectric constants as the wurtzite crystal structure is anisotropic with the interactions with photons in parallel ($\parallel$) and perpendicular ($\perp$) directions with respect to *ab* plane as shown in Fig. S5. A higher dielectric constant reduces the effective force between any two charges in a medium which makes charge separation by photon interaction in that medium easier. All the values of dielectric constants shown in Table S5 are lower than that of Si (11.7) [92]. This lower value of dielectric constant makes these materials harder to achieve a higher efficiency of charge separation due to weakly screened Coulomb attraction [123].

The complex dielectric functions calculated using HSE06 functional for all the five members of $Mg_xZn_{1-x}SnN_2$ alloy system in $\parallel$- and $\perp$-directions are shown in Figs. S6 and S7 respectively. In both directions, the real part shows first peak around the band gap of each alloy. Likewise, the imaginary part starts to rise after the band gap in each alloy. All the other peaks can be attributed to inter-band transitions. The overall behavior of complex dielectric function in both directions is similar in both real and imaginary components. After a few rising peaks, the real part starts to decline, reaches a negative extreme and starts rising again settling down asymptotically in a lower value than the dielectric constant. Moreover, the imaginary part also rises to a point where the real part is about zero and starts declining again finally touching the zero point. The touching of zero mark in imaginary part and final asymptote behavior of the real part happens simultaneously. The right panels in both Figs. S6 and S7 provide a detailed picture of the complex dielectric function around the visible range (1.63 eV–3.26 eV). Both the real and imaginary parts are observed to be slowly rising and peaking at the band gap area.
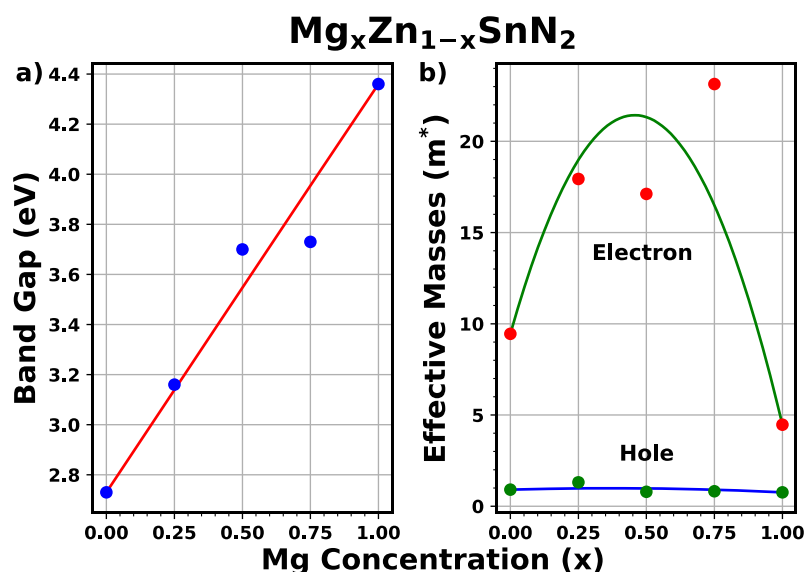
$Mg_xZn_{1-x}SnN_2$

Fig. 1. a) Electronic bandgaps, and b) effective masses of $Mg_xZn_{1-x}SnN_2$ alloys calculated using the hybrid HSEO6 functional. Here, points appear for calculated data whereas curves sketch fitting based on a bowing parameter as defined in Eq. (2).
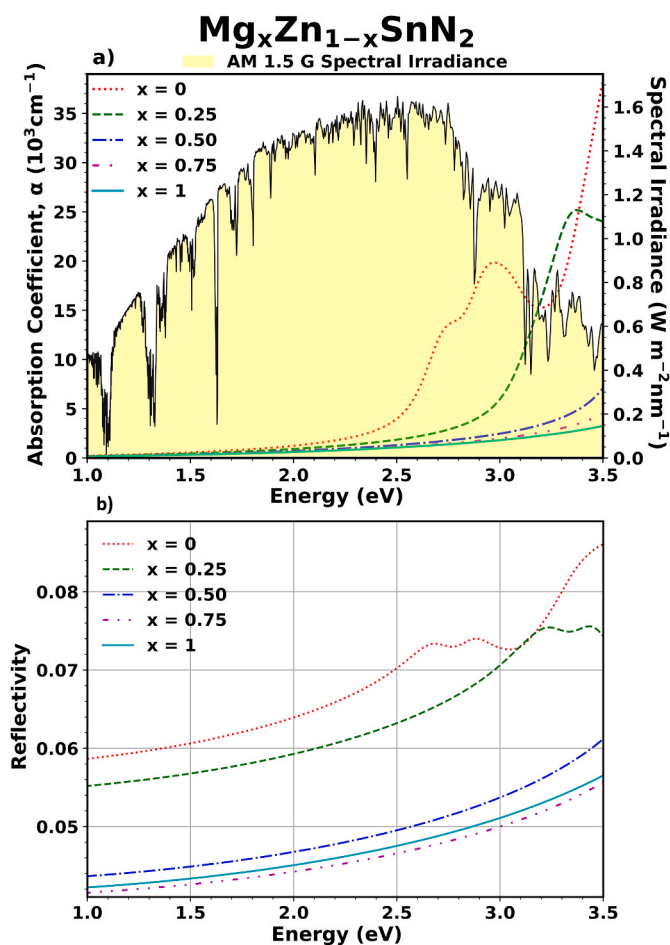

Fig. 2. Absorption coefficient, α (top panel) and reflectivity (bottom panel) curves, left axis, of $Mg_xZn_{1-x}SnN_2$ alloys computed using the hybrid HSE06 functional. Standard AM 1.5 G solar spectral irradiance [124], right axis, is illustrated in the yellow shaded area along with absorption curve. (For interpretation of the references to colour in this figure legend, the reader is referred to the Web version of this article.)

Fig. 2 shows plots of absorption coefficient and reflectivity versus photon energy for all the five members of the $Mg_xZn_{1-x}SnN_2$ alloy system, where average of both directions was considered. For comparison, the spectral irradiance of the AM 1.5 G spectrum [124] is also plotted along with the absorption coefficient. There is no significant absorption in any of the five members of the alloy in the visible region. For an efficient solar cell, the absorption coefficient must be around 10^5 cm^{-1} as observed in CdSe$_x$Te$_{1-x}$ [44], but these materials have only about 10^3 cm^{-1}. However, the absorption slowly rises for the higher photon energy for all the members. For ($x = 0.00$) and ($x = 0.25$), a quick spike in the absorption ($\sim 10^4$ cm^{-1}) is seen in the visible range once they approach their band gaps. Characteristics of the reflectivity curves are equivalent to the absorption curves. The reflectivity for this alloy system is roughly between (4 − 9)%. However, the widely used solar material CdSe$_x$Te$_{1-x}$ has reflectivity around (15 − 31)%. Thus, this $Mg_xZn_{1-x}SnN_2$ alloy system with a lower reflectivity in par with a considerable absorption is also a material candidate for absorber layer of solar cells.

4. Conclusion

We have computationally studied the structural, energetic, mechanical, vibrational, and opto-electronic properties of $Mg_xZn_{1-x}SnN_2$ alloy system utilizing DFT and beyond. Most of our results are predictive in nature for a random disordered crystal structure as there is not much experimental work in the intermediate members of this alloy system. We have observed that the difference between lattice constants in between all the members of the alloy is less than 1 %. This fact helps the alloy to be miscible in all the ranges of concentration, x. The formation energy decreases with the increment in Mg concentration. Band gap increases linearly with increasing Mg concentration. Hole effective masses are about an order of magnitude lower than electron effective masses in these materials. Effective absorptivity with a lower reflection makes this alloy system a good absorber of solar irradiation. Other than ($x = 0.00$), the other four members of the alloy have comparable mechanical properties. This alloy system has very high hardness values while compared to the existing hard coating materials. All the members of this alloy system are mechanically stable, however, ($x = 0.25$) and ($x = 0.50$) are not vibrationally stable. Phonon-phonon interaction may stabilize these materials at room temperature. Finally, all the five members of the alloy are good candidates as window layers of solar cells owing to their large band gaps.

Disclaimer

The views and conclusions contained herein are those of the authors and should not be interpreted as necessarily representing the official policies or endorsements, either expressed or implied, of Air Force Research Laboratory or the U.S. Government.

Declaration of competing interest

The authors declare that they have no known competing financial interests or personal relationships that could have appeared to influence the work reported in this paper.

Data availability

Data will be made available on request.

Acknowledgement

Appendix A. Supplementary data

Supplementary data to this article can be found online at https://doi.org/10.1016/j.matchemphys.2022.126995.

References

[1] W. Shockley, H.J. Queisser, Detailed balance limit of efficiency of p-n junction solar cells, J. Appl. Phys. 32 (3) (1961) 510–519.

[2] S.A. Hadi, E.A. Fitzgerald, A. Nayfeh, Theoretical efficiency limit for a two-terminal multi-junction "step-cell" using detailed balance method, J. Appl. Phys. 119 (7) (2016), 073104.

[3] V. Wang, et al., Tunable band gaps of $In_xGa_{1-x}N$ alloys: from bulk to two-dimensional limit, J. Phys. Chem. C 122 (12) (2018) 6930–6942.

[4] J.W. Orton, C.T. Foxon, Group III nitride semiconductors for short wavelength light-emitting devices, Rep. Prog. Phys. 61 (1) (1998) 1–75.

[5] J. Wu, et al., Superior radiation resistance of $In_{1-x}Ga_xN$ alloys: full-solar-spectrum photovoltaic material system, J. Appl. Phys. 94 (10) (2003) 6477–6482.

[6] I.h. Ho, G.B. Stringfellow, Solid phase immiscibility in GaInN, Appl. Phys. Lett. 69 (18) (1996) 2701–2703.

[7] A. Khan, Laser diodes go green, Nat. Photonics 3 (8) (2009) 432–434.

[8] B. Gil, III-Nitride Semiconductors and their Modern Devices 18, OUP Oxford, 2013.

[9] S.R. Bauers, et al., Ternary nitride semiconductors in the rocksalt crystal structure, Proc. Natl. Acad. Sci. USA 116 (30) (2019) 14829–14834.

[10] A. Punya, T.R. Paudel, W.R.L. Lambrecht, Electronic and lattice dynamical properties of $II-IV-N_2$ semiconductors, Phys. Status Solidi C 8 (7–8) (2011) 2492–2499.

[11] A. Osinsky, et al., New concepts and preliminary results for SiC bipolar transistors: $ZnSiN_2$ and $ZnGeN_2$ heterojunction emitters, in: Proceedings 2000 IEEE/Cornell Conference on High Performance Devices (Cat. No.00CH37122), 2000.

[12] P. Narang, et al., Bandgap tunability in $Zn(Sn,Ge)N_2$ semiconductor alloys, Adv. Mater. 26 (8) (2014) 1235–1241.

[13] N. Yamada, et al., *Band gap-tunable (Mg, Zn)SnN₂ earth-abundant Alloys with a wurtzite structure*, Appl. Electron. Mater. 3 (11) (2021) 4934–4942.

[14] F. Kawamura, et al., Synthesis of a novel rocksalt-type ternary nitride semiconductor $MgSnN_2$ using the metathesis reaction under high pressure, Eur. J. Inorg. Chem. (5) (2020) 446–451, 2020.

[15] R.A. Makin, et al., Alloy-free band gap tuning across the visible spectrum, Phys. Rev. Lett. 122 (25) (2019) 256403.

[16] A.L. Greenaway, et al., Combinatorial synthesis of magnesium tin nitride semiconductors, J. Am. Chem. Soc. 142 (18) (2020) 8421–8430.

[17] M. Kute, et al., Cation-size mismatch as a predictive descriptor for structural distortion, configurational disorder, and valence-band splitting in $II-IV-N_2$ semiconductors, Appl. Phys. Lett. 119 (13) (2021) 132104.

[18] S. Lyu, W.R.L. Lambrecht, *Quasiparticle self-consistent GW band structures of Mg-IV-N₂ compounds: The role of semicore d states*, Solid State Commun. 299 (2019) 113664.

[19] A.P. Jaroenjittichai, W.R.L. Lambrecht, Electronic band structure of $Mg-IV-N_2$ compounds in the quasiparticle-self-consistent GW approximation, Phys. Rev. B 94 (12) (2016) 125201.

[20] B.B. Dumre, D. Gall, S.V. Khare, *Stability, and electronic and optical properties of ternary nitride phases of MgSnN₂: a first-principles study*, J. Phys. Chem. Solid. 153 (2021) 110011.

[21] S. Lany, et al., Monte Carlo simulations of disorder in $ZnSnN_2$ and the effects on the electronic structure, Phys. Rev. Mater. 1 (2017), 035401.

[22] F. Alnjiman, et al., Theoretical and experimental approaches for the determination of functional properties of $MgSnN_2$ thin films, Sol. Energy Mater. Sol. Cell. 244 (2022) 111797.

[23] N. Yamada, et al., Composition-dependent properties of wurtzite-type $Mg_{1+x}Sn_{1-x}N_2$ epitaxially grown on GaN(001) templates, Appl. Electron. Mater. 3 (3) (2021) 1341–1349.

[24] A. Punya, W.R.L. Lambrecht, M. van Schilfgaarde, Quasiparticle band structure of $Zn-IV-N_2$ compounds, Phys. Rev. B 84 (16) (2011) 165204.

[25] D.D. Le, T.S. Ngo, S.-K. Hong, Growth of single crystal non-polar $(112\bar{0})$ $ZnSnN_2$ films on sapphire substrate, Appl. Surf. Sci. 481 (2019) 819–824.

[26] D.D. Le, et al., Epitaxial growth of bandgap tunable $ZnSnN_2$ films on (0001) Al_2O_3 substrates by using a ZnO buffer, Cryst. Growth Des. 18 (3) (2018) 1385–1393.

[27] D. Fang, Y. Li, Structural, electronic, and optical properties of ZnO: $ZnSnN_2$ compounds for optoelectronics and photocatalyst applications, Phys. Lett. 384 (26) (2020) 126670.

[28] N. Feldberg, et al., $ZnSnN_2$: a new earth-abundant element semiconductor for solar cells, in: 2012 38th IEEE Photovoltaic Specialists Conference, 2012.

[29] A.N. Fioretti, et al., Combinatorial insights into doping control and transport properties of zinc tin nitride, J. Mater. Chem. C 3 (42) (2015) 11017–11028.

[30] K. Javaid, et al., Band offset engineering in $ZnSnN_2$-based heterojunction for low-cost solar cells, ACS Photonics 5 (6) (2018) 2094–2099.

[31] M.R. Karim, H. Zhao, Design of $InGaN-ZnSnN_2$ quantum wells for high-efficiency amber light emitting diodes, J. Appl. Phys. 124 (3) (2018), 034303.

[32] R.A. Makin, et al., Order parameter and band gap of $ZnSnN_2$, in: 2018 IEEE 7th World Conference on Photovoltaic Energy Conversion (WCPEC) (A Joint Conference of 45th IEEE PVSC, 28th PVSEC & 34th EU PVSEC), 2018.

[33] F. Oba, Y. Kumagai, Design and exploration of semiconductors from first principles: a review of recent advances, APEX 11 (6) (2018), 060101.

[34] A. Punya, W.R.L. Lambrecht, Band offsets between $ZnGeN_2$, GaN, ZnO, and $ZnSnN_2$ and their potential impact for solar cells, Phys. Rev. B 88 (7) (2013), 075302.

[35] R. Qin, et al., Semiconducting $ZnSnN_2$ thin films for $Si/ZnSnN_2$ p-n junctions, Appl. Phys. Lett. 108 (14) (2016) 142104.

[36] T.R. Paudel, W.R.L. Lambrecht, First-principles calculations of elasticity, polarization-related properties, and nonlinear optical coefficients in $Zn-IV-N_2$ compounds, Phys. Rev. B 79 (24) (2009) 245205.

[37] G. Kresse, J. Furthmuller, Efficiency of ab-initio total energy calculations for metals and semiconductors using a plane-wave basis set, Comput. Mater. Sci. 6 (1) (1996) 15–50.

[38] G. Kresse, J. Furthmuller, Efficient iterative schemes for ab initio total-energy calculations using a plane-wave basis set, Phys. Rev. B 54 (16) (1996) 11169–11186.

[39] G. Kresse, J. Hafner, Ab initio molecular dynamics for liquid metals, Phys. Rev. B 47 (1) (1993) 558–561.

[40] G. Kresse, D. Joubert, From ultrasoft pseudopotentials to the projector augmented-wave method, Phys. Rev. B 59 (3) (1999) 1758–1775.

[41] J.P. Perdew, et al., Erratum: atoms, molecules, solids, and surfaces: applications of the generalized gradient approximation for exchange and correlation, Phys. Rev. B 48 (7) (1993) 4978.

[42] J.P. Perdew, et al., Atoms, molecules, solids, and surfaces: applications of the generalized gradient approximation for exchange and correlation, Phys. Rev. B 46 (11) (1992) 6671–6687.

[43] P.E. Blochl, Projector augmented-wave method, Phys. Rev. B 50 (24) (1994) 17953–17979.

[44] B.B. Dumre, et al., Improved optoelectronic properties in $CdSe_xTe_{1-x}$ through controlled composition and short-range order, Sol. Energy 194 (2019) 742–750.

[45] V.T. Barone, et al., Optoelectronic and mechanical properties of the orthogonal and tetragonal $Cu_2CdGe(S_xSe_{1-x})_4$ semiconducting system via first principles methods, J. Appl. Phys. 131 (20) (2022) 205701.

[46] I. Efthimiopoulos, et al., Pressure-induced transition in the multiferroic $CoCr_2O_4$ spinel, Phys. Rev. B 92 (6) (2015).

[47] S.V. Khare, T.L. Einstein, N.C. Bartelt, Dynamics of step doubling: simulations for a simple model and comparison with experiment, Surf. Sci. 339 (3) (1995) 353–362.

[48] A.W. Ghosh, S.V. Khare, Rotation in an asymmetric multidimensional periodic potential due to colored noise, Phys. Rev. Lett. 84 (23) (2000) 5243.

[49] J.L. Roehl, et al., Binding sites and diffusion barriers of a Ga adatom on the GaAs (001)-c(4X4) surface from first-principles computations, Phys. Rev. B 82 (16) (2010).

[50] S. Kodambaka, et al., Size-dependent detachment-limited decay kinetics of two-dimensional TiN islands on TiN(111), Phys. Rev. Lett. 89 (17) (2002) 176102.

[51] P.P. Gunaicha, et al., Structural, energetic and elastic properties of Cu_2ZnSn $(S_xSe_{1-x})_4$ ($x= 1, 0.75, 0.5, 0.25, 0$) alloys from first-principles computations, Sol. Energy 102 (2014) 276–281.

[52] N. Jiang, et al., An ab initio computational study of pure Zn_3N_2 and its native point defects and dopants Cu, Ag and Au, Thin Solid Films 564 (2014) 331–338.

[53] Y.J. Wang, et al., Thermal equation of state of silicon carbide, Appl. Phys. Lett. 108 (6) (2016) 5.

[54] S.V. Khare, T.L. Einstein, Energetics of steps and kinks on Ag and Pt using equivalent crystal theory (ECT), Surf. Sci. 314 (1) (1994) L857–L865.

[55] A. Jain, et al., Commentary: the Materials Project: a materials genome approach to accelerating materials innovation, Apl. Mater. 1 (1) (2013) 11.

[56] A. Zunger, et al., Special quasirandom structures, Phys. Rev. Lett. 65 (3) (1990) 353–356.

[57] J.A. Warner, et al., Ab initio calculations for properties of MAX phases Ti_2TlC, Zr_2TlC, and Hf_2TlC, Appl. Phys. Lett. 88 (10) (2006) 101911.

[58] S. Kodambaka, et al., Dislocation-driven surface dynamics on solids, Nature 429 (6987) (2004) 49–52.

[59] A. van de Walle, Multicomponent multisublattice alloys, nonconfigurational entropy and other additions to the Alloy Theoretic Automated Toolkit, Calphad Comput. Coupling Phase Diagrams Thermochem. 33 (2) (2009) 266–278.

[60] A. van de Walle, M. Asta, Self-driven lattice-model Monte Carlo simulations of alloy thermodynamic properties and phase diagrams, Model. Simulat. Mater. Sci. Eng. 10 (5) (2002) 521–538.

[61] A. van de Walle, M. Asta, G. Ceder, The alloy theoretic automated toolkit: a user guide, Calphad Comput. Coupling Phase Diagrams Thermochem. 26 (4) (2002) 539–553.

[62] A. van de Walle, G. Ceder, Automating first-principles phase diagram calculations, J. Phase Equil. 23 (4) (2002) 348–359.

[63] A. van de Walle, et al., Efficient stochastic generation of special quasirandom structures, Calphad 42 (2013) 13–18.

[64] I.S. Khare, et al., Electronic, optical, and thermoelectric properties of sodium pnictogen chalcogenides: a first principles study, Comput. Mater. Sci. 183 (2020) 109818.

[65] V. Adhikari, et al., First-principles study of mechanical and magnetic properties of transition metal (M) nitrides in the cubic M_4N structure, J. Phys. Chem. Solid. 120 (2018) 197–206.

[66] N.J. Szymanski, et al., Prediction of improved magnetization and stability in $Fe_{16}N_2$ through alloying, J. Appl. Phys. 126 (9) (2019) 093903.

[67] X. Wu, D. Vanderbilt, D.R. Hamann, Systematic treatment of displacements, strains, and electric fields in density-functional perturbation theory, Phys. Rev. B 72 (3) (2005), 035105.

[68] V. Adhikari, et al., First principles investigation into the phase stability and enhanced hardness of TiN-ScN and TiN-YN alloys, Thin Solid Films 688 (2019) 137284.

[69] N.J. Szymanski, et al., Dynamical stabilization in delafossite nitrides for solar energy conversion, J. Mater. Chem. 6 (42) (2018) 20852–20860.

[70] K. Balasubramanian, S.V. Khare, D. Gall, Energetics of point defects in rocksalt structure transition metal nitrides: thermodynamic reasons for deviations from stoichiometry, Acta Mater. 159 (2018) 77–88.

[71] Z. Liu, et al., First-principles phase diagram calculations for the rocksalt-structure quasibinary systems TiN-ZrN, TiN-HfN and ZrN-HfN, J. Phys. Condens. Matter 29 (3) (2016), 035401.

[72] K. Balasubramanian, S. Khare, D. Gall, Vacancy-induced mechanical stabilization of cubic tungsten nitride, Phys. Rev. B 94 (17) (2016) 174111.

[73] K. Zhang, et al., Growth and mechanical properties of epitaxial NbN(001) films on MgO(001), Surf. Coating. Technol. 288 (2016) 105–114.

[74] K. Zhang, et al., Epitaxial $NbxN_{1-x}$(001) layers: growth, mechanical properties, and electrical resistivity, Surf. Coating. Technol. 277 (2015) 136–143.

[75] G. Grimvall, in: E. Wohlfarth (Ed.), Thermophysical Properties of Materials, Ser. Selected Topics in Solid State Physics, North-Holland, Amsterdam, 1986, p. 18.

[76] R. Hill, The elastic behaviour of a crystalline aggregate, Proc. Phys. Soc. 65 (5) (1952) 349–354.

[77] A. Reuss, Berechnung der fließgrenze von mischkristallen auf grund der plastizitätsbedingung für einkristalle, J. Appl. Math. Mech. 9 (1) (1929) 49–58.

[78] X. Zhou, D. Gall, S.V. Khare, Mechanical properties and electronic structure of anti-ReO$_3$ structured cubic nitrides, M_3N, of d block transition metals M: an ab initio study, J. Alloys Compd. 595 (2014) 80–86.

[79] W. Voigt, Lehrbuch der kristallphysik, Teubner Leipzig 962 (1928).

[80] B.B. Dumre, S.V. Khare, Interrelationship of bonding strength with structural stability of ternary oxide phases of $MgSnO_3$: a first-principles study, Physica B: Condens. Matter 637 (2022) 413896.

[81] S.F. Pugh, Xcii. Relations between the elastic moduli and the plastic properties of polycrystalline pure metals, Lond. Edinb. Dublin Phil. Mag. J. Sci. 45 (367) (1954) 823–843.

[82] Y. Tian, B. Xu, Z. Zhao, Microscopic theory of hardness and design of novel superhard crystals, Int. J. Refract. Metals Hard Mater. 33 (2012) 93–106.

[83] Z.T.Y. Liu, D. Gall, S.V. Khare, Electronic and bonding analysis of hardness in pyrite-type transition-metal pernitrides, Phys. Rev. B 90 (13) (2014) 134102.

[84] Z.T.Y. Liu, et al., First-principles investigation of the structural, mechanical and electronic properties of the NbO-structured 3d, 4d and 5d transition metal nitrides, Comput. Mater. Sci. 84 (2014) 365–373.

[85] Z.T.Y. Liu, et al., Structural, mechanical and electronic properties of 3d transition metal nitrides in cubic zincblende, rocksalt and cesium chloride structures: a first-principles investigation, J. Phys. Condens. Matter 26 (2) (2014), 025404.

[86] M. Born, On the stability of crystal lattices. I, Math. Proc. Camb. Phil. Soc. 36 (2) (1940) 160–172.

[87] J. Paier, et al., Screened hybrid density functionals applied to solids, J. Chem. Phys. 124 (15) (2006) 154709.

[88] A.V. Krukau, et al., Influence of the exchange screening parameter on the performance of screened hybrid functionals, J. Chem. Phys. 125 (22) (2006) 224106.

[89] N.J. Szymanski, et al., Electronic and optical properties of vanadium oxides from first principles, Comput. Mater. Sci. 146 (2018) 310–318.

[90] Z.T.Y. Liu, et al., Transparency enhancement for $SrVO_3$ by $SrTiO_3$ mixing: a first-principles study, Comput. Mater. Sci. 144 (2018) 139–146.

[91] M. Gajdoš, et al., Linear optical properties in the projector-augmented wave methodology, Phys. Rev. B 73 (4) (2006), 045112.

[92] C. Kittel, Introduction to Solid State Physics, John Wiley&Sons, New York, 2005 (Inc).

[93] G.K.H. Madsen, J. Carrete, M.J. Verstraete, BoltzTraP2, a program for interpolating band structures and calculating semi-classical transport coefficients, Comput. Phys. Commun. 231 (2018) 140–145.

[94] G.K.H. Madsen, D.J. Singh, BoltzTraP. A code for calculating band-structure dependent quantities, Comput. Phys. Commun. 175 (1) (2006) 67–71.

[95] V.L. Deringer, A.L. Tchougreeff, R. Dronskowski, Crystal orbital Hamilton population (COHP) analysis as projected from plane-wave basis sets, J. Phys. Chem. 115 (21) (2011) 5461–5466.

[96] R. Dronskowski, P.E. Blochl, Crystal Orbital Hamilton Populations (COHP). Energy-resolved visualization of chemical bonding in solids based on density-functional calculations, J. Phys. Chem. 97 (33) (1993) 8617–8624.

[97] S. Maintz, et al., Analytic projection from plane-wave and PAW wavefunctions and application to chemical-bonding analysis in solids, J. Comput. Chem. 34 (29) (2013) 2557–2567.

[98] S. Maintz, et al., LOBSTER: a tool to extract chemical bonding from plane-wave based DFT, J. Comput. Chem. 37 (11) (2016) 1030–1035.

[99] S. Maintz, M. Esser, R. Dronskowski, Efficient rotation of local basis functions using real spherical harmonics, Acta Phys. Pol. B 47 (4) (2016) 1165–1175.

[100] N.J. Szymanski, et al., Unconventional superconductivity in 3d rocksalt transition metal carbides, J. Mater. Chem. C 7 (40) (2019) 12619–12632.

[101] Z.T.Y. Liu, et al., First-principles phase diagram calculations for the rocksalt-structure quasibinary systems TiN-ZrN, TiN-HfN and ZrN-HfN, J. Phys. Condens. Matter 29 (3) (2017), 035401.

[102] G. Henkelman, A. Arnaldsson, H. Jónsson, A fast and robust algorithm for Bader decomposition of charge density, Comput. Mater. Sci. 36 (3) (2006) 354–360.

[103] E. Sanville, et al., Improved grid-based algorithm for bader charge allocation, J. Comput. Chem. 28 (5) (2007) 899–908.

[104] W. Tang, E. Sanville, G. Henkelman, A grid-based Bader analysis algorithm without lattice bias, J. Phys. Condens. Matter 21 (8) (2009) 084204.

[105] M. Yu, D.R. Trinkle, Accurate and efficient algorithm for Bader charge integration, J. Chem. Phys. 134 (6) (2011), 064111.

[106] A. Togo, I. Tanaka, First principles phonon calculations in materials science, Scripta Mater. 108 (2015) 1–5.

[107] E. Kasper, et al., Test of Vegard's law in thin epitaxial SiGe layers, J. Cryst. Growth 157 (1) (1995) 68–72.

[108] T.D. Veal, et al., Band gap dependence on cation disorder in $ZnSnN_2$ solar absorber, Adv. Energy Mater. 5 (24) (2015) 1501462.

[109] T.R. Paudel, W.R.L. Lambrecht, First-principles study of phonons and related ground-state properties and spectra in $Zn-IV-N_2$ compounds, Phys. Rev. B 78 (11) (2008) 115204.

[110] F. Kawamura, et al., Synthesis of $ZnSnN_2$ crystals via a high-pressure metathesis reaction, Cryst. Res. Technol. 51 (3) (2016) 220–224.

[111] P. Pyykkö, Additive covalent radii for single-, double-, and triple-bonded molecules and tetrahedrally bonded crystals: a summary, J. Phys. Chem. 119 (11) (2015) 2326–2337.

[112] J.P. Zanatta, et al., Growth of HgCdTe and CdTe(331)B on germanium substrate by molecular beam epitaxy, Appl. Phys. Lett. 71 (20) (1997) 2984–2986.

[113] S. Cole, M. Brown, A.F.W. Willoughby, The microhardness of $Cd_xHg_{1-x}Te$, J. Mater. Sci. 17 (7) (1982) 2061–2066.

[114] K. Balasubramanian, S.V. Khare, D. Gall, Valence electron concentration as an indicator for mechanical properties in rocksalt structure nitrides, carbides and carbonitrides, Acta Mater. 152 (2018) 175–185.

[115] B.D. Ozsdolay, et al., Cubic β-WN_x layers: growth and properties vs N-to-W ratio, Surf. Coating. Technol. 304 (2016) 98–107.

[116] S. Kodambaka, et al., Absolute orientation-dependent anisotropic TiN(111) island step energies and stiffnesses from shape fluctuation analyses, Phys. Rev. B 67 (3) (2003), 035409.

[117] J. Bareno, et al., Orientation-dependent mobilities from analyses of two-dimensional TiN (111) island decay kinetics, Thin Solid Films 510 (1–2) (2006) 339–345.

[118] I. Khatri, et al., Correlating structure and orbital occupation with the stability and mechanical properties of 3d transition metal carbides, J. Alloys Compd. 891 (2022) 161866.

[119] R.M. Hornreich, et al., Phonon band gaps, J. Phys. 7 (3) (1997) 509–519.
[120] A.L. Allred, E.G. Rochow, A scale of electronegativity based on electrostatic force, J. Inorg. Nucl. Chem. 5 (4) (1958) 264–268.
[121] M.A. Green, Intrinsic concentration, effective densities of states, and effective mass in silicon, J. Appl. Phys. 67 (6) (1990) 2944–2954.
[122] B.E. Warren, B.L. Averbach, B.W. Roberts, Atomic size effect in the X-ray scattering by alloys, J. Appl. Phys. 22 (12) (1951) 1493–1496.
[123] Hamam, K.J.T., Organic solar cells based on high dielectric constant materials: an approach to increase efficiency, in department of physics. 2013, Western Michigan University: Graduate College at ScholarWorks at Western Michigan University. p. 107.
[124] N.R.E. Laboratory, Reference Air mass 1.5 spectra, Available from: https://www.nrel.gov/grid/solar-resource/spectra-am1.5.html, 2003.
[125] Ohio Supercomputer Center, 1987.